The Cryosphere
Open Access
Discussions

Imaging air volume fraction in sea ice using non-destructive X-ray tomography

O. Crabeck[1], R. J. Galley[1], B. Delille[2], B. G. T. Else[3], N.-X. Geilfus[4], M. Lemes[1], M. Des Roches[5], P. Francus[5], J.-L. Tison[6], and S. Rysgaard[1,4,7]

[1]Department of Geological Sciences, Centre for Earth Observation, University of Manitoba, Winnipeg, Manitoba, Canada
[2]Unité d'Océanographie Chimique, MARE, Université de Liège, Liège, Belgium
[3]Department of Geography, University of Calgary, Calgary, Alberta, Canada
[4]Arctic Research Centre, Aarhus University, Aarhus, Denmark
[5]Centre Eau terre et Environement, INRS-Été-Quebec, Quebec, Canada
[6]Laboratoire de Glaciologie, DSTE, Université Libre de Bruxelles, Bruxelles, Belgium
[7]Greenland Climate Research Centre, Greenland Institute of Natural Resources, Nuuk, Greenland

Title Page

Abstract	Introduction
Conclusions	References
Tables	Figures

| ◄◄ | ►► |
| ◄ | ► |

Back | Close

Full Screen / Esc

Printer-friendly Version

Interactive Discussion

Abstract

Although the presence of a gas phase in sea ice creates the potential for gas exchange with the atmosphere, the distribution of gas bubbles and transport of gases within the sea ice are still poorly understood. Currently no straightforward technique exists to measure the vertical distribution of air volume fraction in sea ice. Here, we present a new fast and non-destructive X-ray computed tomography technique to quantify the air volume fraction and produce separate 3-D images of air-volume inclusions in sea ice. The technique was performed on relatively thin (4–22 cm) sea ice collected from an experimental ice tank. While most of the internal layers showed air-volume fractions < 2 %, the ice–air interface (top 2 cm) systematically showed values up to 5 %. We suggest that the air volume fraction is a function of both the bulk ice gas saturation factor and the size of the brine channel. We differentiate micro bubbles (ø < 1 mm), large bubbles (1 < ø < 5 mm) and macro bubbles (ø > 5 mm). While micro bubbles were the most abundant type of air inclusions, most of the air porosity observed resulted from the presence of large and macro bubbles. The ice microstructure (granular and columnar) as well as the permeability state of ice are important factors controlling the air volume fraction. The technique developed is suited for studies related to gas transport and bubble migration and can help considerably improving parameterization of these processes in sea ice biogeochemical models.

1 Introduction

Sea ice is a multi-phase system consisting of ice crystals, salt precipitates, brine, and gas bubbles (i.e. air inclusions). The abundance and morphology of brine and air inclusions are strongly dependent on the temperature and salinity of the sea ice (Cox and Weeks, 1983; Weeks and Ackley, 1986). Microscale studies of sea ice inclusions have in large part focused on the formation and morphology of brine inclusions (as pockets and or channels) (e.g. Bennington, 1967; Bock and Eicken, 2005; Cole and Shapiro,

1998; Cox and Weeks, 1975; Eicken et al., 2000; Eide and Martin, 1975; Galley et al., 2015a; Hunter et al., 2009; Notz and Worster, 2008). Inclusions in large part control the transfer of heat, salt, gases, and radiation between the ocean and atmosphere (Light et al., 2003). Brine and air inclusions in sea ice also affect the optical and electromagnetic properties of sea ice, and are often sites of biological activity (Fritsen et al., 1994; Krembs et al., 2000; Vancoppenolle et al., 2014).

Studies on the formation and morphology of gas inclusions and gas transport within sea ice are sparse. The air porosity quantitatively defined by the air volume fraction (V_a %) has generally been neglected in past work; it has long been assumed that gas species in sea ice were dissolved in brine and subject to the same processes as brine inclusions, and that the air volume fraction is very small compared to the brine volume fraction. Mushy layer theory, whose equations are now used as the physical basis for liquid exchange processes within sea ice neglect the presence of air inclusions (Feltham et al., 2006; Worster, 1992, 1997; Rees Jones and Worster, 2013). Omission of air inclusions in sea ice research propagates a lack of understanding of gas transport within sea ice, though studies in the last decade have revealed substantial CO_2 fluxes at the sea ice–atmosphere interface (Semiletov et al., 2004; Zemmelink et al., 2006; Delille et al., 2014; Geilfus et al., 2014, 2015; Normura et al., 2006, 2010, 2013). It was also recently argued that a major part of the natural gases (O_2, N_2, Ar) as well as methane (CH_4) reside in the gas phase inside bubbles in sea ice rather than dissolved in the brine (Zhou et al., 2013; Moreau et al., 2014; Crabeck et al., 2014a, b). Therefore the physical properties and processes of air inclusions in sea ice can potentially control the sea ice–atmosphere exchange of gases. The most important process leading to the formation of air inclusions from entrapped brine is brine volume reduction by freezing (Zhou et al., 2013; Crabeck et al., 2014a, b; Moreau et al., 2014). Increasing brine salinity during winter due to sea ice temperature reduction results in reduced gas solubility causing super-saturation (the *brine concentration effect*), which leads to bubble formation if the sum of the partial pressures of all the dissolved gases is higher than the local hydrostatic pressure.

Imaging air volume fraction in sea ice using non-destructive X-ray tomography

O. Crabeck et al.

Limitations of current methods have resulted in a lack of detailed descriptions of sea ice air inclusions in the literature. The current methods provide inadequate profiles of the vertical distribution of air inclusions in sea ice, especially in the context of ocean–sea ice–atmosphere exchange of gas. The sea ice air-volume fraction is most often determined empirically from bulk temperature, salinity and density measurements (after Cox and Weeks, 1983). However, small errors associated with sea ice density measurements result in large errors in the calculated air-volume fraction. Perovich and Gow (1996), and Light et al. (2003) employed sea ice sections imaged using transmitted light to describe air inclusions within sea ice, given the caveats that undisturbed microstructure required careful thermal control, size may be limited, and the distinction between gas and brine can be ambiguous in transmitted images. Another approach is high resolution measurements of the total gas content along a vertical profile using techniques initially developed for continental ice cores (melting-refreezing and toepler pump extraction or summing individual gases concentrations measured using gas chromatography (GC) (Tison et al., 2002). These techniques however operate under vacuum, and therefore collect both the dissolved and gaseous phases. Also, this technique does not provide information on the morphology of the bubble content. A third approach used previously is to melt the ice sample in a gas tight container and quantify total gas volume (Rysgaard and Glud, 2004). A problem with this approach, however, is that gasses will equilibrate to the new "bulk" situation of temperature and salinity and hence not represent the actual gas volume at in situ conditions.

We propose a methodological advancement employing computed tomography (CT) X-ray imaging for measurement of air inclusions within sea ice. For many years CT X-ray has been widely used as a medical diagnostic tool. This non-invasive technique has largely contributed to the study of rock fractures and rock porosity, and has recently been applied to the sea ice field, advancing percolation theory for the brine system (Golden et al., 2007; Pringle et al., 2009). Here we present high-resolution profiles of the distribution of air inclusions in sea ice, which are derived from CT X-ray images of whole ice cores at the sub-millimeter scale in three dimensions. A detailed statistical

Title Page

Abstract	Introduction
Conclusions	References
Tables	Figures

Back | Close

Full Screen / Esc

Printer-friendly Version

Interactive Discussion

analysis of the air volume fraction in experimental sea ice is presented, as well as comparisons to the air volume equations of Cox and Weeks (1983) and measurement of total gas content. Throughout this work, we highlight the parameters and processes influencing the air porosity (air volume fraction, V_a).

2   Methods

2.1   Sea ice Environmental Research Facility (SERF)

The Sea-ice Environmental Research Facility (SERF) at the University of Manitoba (Winnipeg, Canada) is an in-ground concrete pool with dimensions of 23.3 m (length) × 9.2 m (width) × 2.75 m (depth). It is filled each year with seawater formulated on site to closely replicate the chemistry of Arctic surface seawater (e.g. Hare et al., 2013; Geilfus et al., 2013; Rysgaard et al., 2014). In January 2013 an experiment was initiated from open water conditions, where sea ice was allowed to grow to 22 cm thick between 13 and 26 January. Ice cores were collected on 14, 16 and 25 January to measure bulk ice gas composition, temperature, salinity, and density, and for imaging in three-dimensions using a computed tomography X-ray instrument.

2.2   Sea ice core: temperature, salinity and texture

At least four ice cores were extracted on each sampling occasion using a Mark II core barrel with an internal diameter of 9 cm (Kovacs Ent., Lebanon, USA). One of the cores was destructively interrogated to measure an in situ ice temperature profile at a depth resolution of 2 cm using a calibrated probe (Testo 720, precision ±0.1 °C) inserted into pre-drilled holes with the same diameter as the probe perpendicular to the ice core depth axis. The second ice core extracted was immediately cut into 2 cm slices which were stored in polyethylene buckets and left to melt close to 0 °C. Bulk ice salinity of the melt of these 2 cm sections was derived from sample conductivity and temperature measured with a porTable conductivity meter (Orion Star Series Meter WP-84TP,

Imaging air volume fraction in sea ice using non-destructive X-ray tomography

O. Crabeck et al.

Title Page

Abstract	Introduction
Conclusions	References
Tables	Figures

Back   Close

Full Screen / Esc

Printer-friendly Version

Interactive Discussion

precision ±0.1) using the equations of Grasshoff et al. (1983). For further analyses including gas composition and CT X-ray imaging, the third and fourth cores were immediately wrapped in polyethylene bags and stored at −20 °C in the dark to ensure brine/gas immobilization and to inhibit biological processes (Eicken, 1991).

2.3 Gas composition

The bulk ice concentration of Argon (Ar), oxygen (O_2) and nitrogen (N_2) expressed in µmol L^{-1} ice were analyzed by GC. The dry-crushing technique as developed for gas measurements in continental ice (e.g. Raynaud et al., 1982) was used to extract the gas phase from the sea ice samples in a cold laboratory at −25 °C. Specifically, each ice core sample for gas composition was cut in 5 cm sections. 60 g of each section were put into a vessel together with stainless steel beads. The vessel was evacuated to 10^{-3} torr, and then fixed to an ice crusher (after Raynaud et al., 1982; Stefels et al., 2012). The stainless steel beads impact the ice block during the shaking process, so that the ice is crushed into a fine powder. After crushing, the vessel was kept at −50 °C in a cold ethanol bath and connected to a gas chromatograph (Trace GC) equipped with a thermal conductivity detector for concentration analyses (Skoog et al., 1997). We used AlphagazTM2 He (Air Liquid –P0252) as the carrier gas and a 22 mL packed column (Mole Sieve 5A 80/100; 5 m × 1/8″). Gas collected included both the gas bubbles in the ice and the dissolved phase within the brine (which cannot be differentiated using this method). The total gas content (mL L^{-1} ice) was derived from the sum of O_2, N_2 and Ar concentrations (initially expressed in µmol L^{-1} ice).

The saturation level of a gas affects bubble nucleation in brine inclusions and is therefore viewed as a crucial parameter determining gas flux at the ice–air interface. Theoretically, nucleation occurs when the sum of the partial pressures of the dissolved gases is higher than the local hydrostatic pressure. We therefore compared (i) the evolution of gas concentrations measured in bulk ice; $C_{\text{bulk ice}}$ to (ii) the theoretical inventory predicted by the solubility in brine at atmospheric saturation; $C_{\text{Saturation}}$ (i.e.

Title Page

Abstract | Introduction

Conclusions | References

Tables | Figures

|◄ | ►|

◄ | ►

Back | Close

Full Screen / Esc

Printer-friendly Version

Interactive Discussion

the maximum concentration of O_2, N_2 and Ar in the dissolved phase when the brine is not supersaturated, Carte, 1961; Lubetkin, 2003; Zhou and et al., 2013). $C_{Saturation}$ is obtained by calculating the temperature and salinity-dependent solubility of O_2, N_2 and Ar in the brine (Garcia and Gordon, 1992; Hamme and Emerson, 2004) and dividing it by the relative brine volume (i.e. the brine volume fraction (V_b), see below) to express it in ml L^{-1} of bulk ice. These relationships are valid for the range of temperature and salinity found in sea ice (Zhou et al., 2013). The ratio of observed concentration in bulk ice ($C_{bulk\ ice}$) to the theoretical saturation concentration in bulk ice ($C_{Saturation}$) defines the saturation factor (SAT_f).

2.4 Bulk ice density

In order to compute the brine volume fraction and the air volume fraction using Cox and Weeks (1983) equations, we measured the bulk ice density with the Mass–Volume technique in a cold lab ($-20\,°C$). Ice core sections were cut into cubes of $5\,cm^3$ and weighed precisely to determine their mass (M). The dimensions of the sample were measured giving their volume (V). The density of the ice (ρ_i) calculated by:

$$\rho_i = \frac{M}{V}.$$

To limit error induced by imperfect sample dimensions, we used a precision diamond wire saw. The length of each edge (the number of edges per cube = 12) was found to deviate from $5\,cm$ by $\pm 0.07\,cm$ on average (total number of edges measured = 96; 8 ice cubes) yielding an average precision for ice density of $\pm 0.020\,g\,cm^{-3}$, due to the cutting process alone.

This common technique is easily applied, but there are several possible sources of error; obtaining a dimensionally perfect ice sample is difficult, and inaccuracies in the measurement of the sample dimensions lead to volume error (Timco and Frederking, 1995).

2.5 Liquid porosity: brine volume fraction

The brine volume was calculated according to Cox and Weeks (1983) using the in situ temperatures, bulk ice salinity data and bulk ice density measurements from the cores. Brine salinity (S_b) was calculated from the in situ sea ice temperatures and the freezing point of seawater (UNESCO, 1978). The brine volume fraction, (V_b, expressed in %), was calculated from the ratio of brine volume and bulk sea ice volume (b/V). In the past literature, sea ice porosity refers solely to the brine volume fraction because the air volume fraction is neglected. In the context of this paper, the terms brine inclusions and brine volume fraction refers to the liquid porosity. We used the permeability threshold of $V_b = 5\%$ following Golden et al. (1998, 2007) to define permeable and impermeable sea ice using the in situ vertical temperatures profiles.

2.6 Ice texture

To describe the ice crystal texture, horizontal thin sections of maximum 10 cm length were produced in a cold lab at $-20\,°C$ using the standard microtome (Leica SM2400) procedure described by Langway (1958) and Tison et al. (2008). Images of these back-lit horizontal thin sections were taken in the cold lab between crossed polarizing sheets with a camera (Nikon Coolpix S200).

2.7 Air porosity: air volume fraction by computed tomography (CT) X-ray imaging

2.7.1 General principle

CT scanning is a non-destructive radiographic approach to examine materials by creating a three-dimensional map of density contrasts. Ice cores were imaged using a third generation Siemens Somatom Volume Access sliding gantry medical CT-Scanner (Siemens SOMATOM Definition AS+ 128) at the Institut National de la Recherche Scientifique (INRS-ETE). Tomograms were acquired continuously every

0.25 mm along each 0.6 mm-thick slice. The U-channels were scanned with X-ray peak energy of 120 kV with 250 mA current. By scanning a core from top to bottom, a three-dimensional "stack" of images was produced by compiling individual transverse slices and longitudinal slices (Fig. 1a), yielding three-dimensional pixel (voxel) volume of 0.25 mm × 0.25 mm × 0.6 mm within square (512 × 512 voxel) images.

Each CT image consists of pixels representing 0.0375 mm^3, whose Hounsfield Unit (HU) value (Hounsfield, 1973) corresponds to linear X-ray attenuation (Duliu, 1999), where higher density and higher atomic numbers result in greater X-ray attenuation. Hounsfield (1973) and Knoll (1989) have described the X-ray technique. Ice core density was calculated in terms of tomographical intensity (TI) (i.e. the HU of each voxel):

$$TI = \left(\frac{\mu}{\mu_w} - 1 \right) \cdot 1000 \qquad (1)$$

where μ is the linear absorption coefficient of the bulk core, and μ_w is the linear absorption coefficient of water. μ is a function of the radiation energy and the atomic number of the core component crossed by the beam and varies in relation to the density of the material. Each pixel contains a HU value and the resulting images are represented in grey scale where darker tones indicate lower density material (e.g. air) (Fig. 1a–c). Density measurements were made relative to water and expressed in HU where water $= 0$ HU and air $= -1000$ HU. For our samples, we observed HU values from -927 to 110 (Fig. 1d). Positive values are related to brine and slightly negative values are related to ice, as pure ice has a theoretical HU value of -84 (Kawamura et al., 1988, 1990). The DICOM-format images obtained from the CT scan were analyzed using a combination of software including OsirisTM, CTan, Matlab and ImageJ 64.

2.7.2 Processing X-ray images and analysis

CTan and ImageJ software were used to quantitatively measure morphometric characteristics of binary (black and white) images. The process of pixel selection (binarization) was performed by means of segmentation or thresholding following the determination

of a region-of-interest (ROI) created by the removal of all pixels not belonging to the core sample (i.e. the sample container, disturbance of the core edges by coring and/or storage, the supporting bench, and surrounding air from each slice). The images were individually examined and ambiguous pixels around the sea ice core sample were also removed. We have eliminated the bottom 1 cm of each imaged ice core due to observed core brine drainage resulting from the coring method. Binarization identified all the pixels representing air, therefore defining the air volume fraction (air porosity, V_a). A three-dimensional orthoslice view as well as two transversal slices of the ice core sample extracted on 16 January are shown in Fig. 1. The bottom of the ice core from which brine drainage occurred during core extraction can be differentiated from the rest of the core sample unaffected by brine loss on both the orthoslice and transversal slice views (Fig. 1a–c).

The number of existing segmentation methods described in the literature exceeds 100. In this study the segmentation algorithms evaluated represent a selection of established thresholding techniques chosen on the basis that they suited a unimodal histogram (e.g. Fig. 1d), and their potential for automated characterization of pore space in geomaterials. Global thresholding was selected on the basis of comparative reviews by Sezgin and Sankur (2004) and Iassonov et al. (2009). Global thresholding may be divided into several subcategories depending on the applied approach. First, there exist global thresholding methods that analyze histogram shape (HS), including HS-Zack and HS-Tsai. HS-Zack utilizes geometrical analysis of the histogram shape (triangulation) (Zack et al., 1977; Rosin, 2001), which assumes a maximum peak (mode) near one end of the histogram and searches towards the other end. HS-Tsai employs peak, valley and maximum curvature measurements of the image histogram to determine the optimum threshold value (Tsai, 1995).

Secondly, segmentation may be accomplished by clustering (CL) methods, which separate background (i.e. ice) and foreground voxels (i.e. air) by approximating the histogram with a combination of two or more statistical distributions. CL-Otsu (Otsu, 1979) is one of the most commonly used of these clustering methods; the goal of

Imaging air volume fraction in sea ice using non-destructive X-ray tomography

O. Crabeck et al.

O. Crabeck et al.

this method is to find a threshold value which minimizes the within-class variances of background and foreground voxel classes, which is equivalent to maximizing the variance between the means of the two clustered classes (Sund and Eilertsen, 2003). The CL-Ridler method (also known as isodata or k-means clustering) uses an iterative approach to find the threshold as the midpoint between means of background and foreground voxels (Ridler and Calvard, 1978).

The third category is based on signal entropy (EN) considerations (Shannon and Weaver, 1948; Pal and Pal, 1989; Pal, 1996) to separate background and foreground voxels. EN-Kapur considers the image foreground and background as two different signal sources and finds the optimum threshold value by maximizing the sum of the foreground and background signal entropies (Kapur et al., 1985). EN-Yen calculates the threshold value by maximizing the entropic correlation between the object and background classes (Yen et al., 1995).

One of the main challenges in comparing segmentation algorithms for X-ray CT images of porous materials is the lack of knowledge of the optimal binarization result. Further, thresholding impacts the image analyses; for example, delineation of an object using HU values will change depending on the HU values of adjacent materials. If an air bubble (HU value = -1000) is adjacent to both ice (HU value = -84) and brine (HU value = 110) the pixel(s) at its boundary will be roughly -540 on the ice-side and -445 on the brine-side. Bubbles smaller than 0.25 mm in diameter may not be properly accounted for because their HU values are drowned out by the surrounding ice pixels due to the resolution of the CT instrument, causing these tiny bubbles to show up as "mixed" pixels with densities a little lower than ice in the CT images. Each segmentation method was tested on the three data sets (633 total image slices). Each method was run on each entire data set, as well as on selected parts of each image set. The results of each method were visually evaluated by comparing the raw and segmented images (Fig. 2a–c) and by computing linear profiles of HU values through cross-sectional images and examining them visually to determine the efficacy of various thresholds in identifying air inclusions (Fig. 2d).

Analysis of variance (ANOVA) demonstrated significant differences between the results of the different thresholding methods ($p < 0.001$). Results shown for one example core in Table 1 indicate that measured porosities are highly dependent on the threshold. Both the En-Yen and the EN-Kapur (max-entropy) algorithms produced high thresholds (-190 and -210 respectively) that detected mixed pixels (< 0.25 mm diameter inclusions) but also introduced noise and speckle in the image (Fig. 2a). The EN-Yen algorithm detected 732 air inclusions in the slice (Fig. 2a), 76 % of which were smaller than one pixel and EN-Kapur detected 502 inclusions, 62 % of which were smaller than one pixel. In contrast, the HS-Zack method (Zack et al., 1997) and the Tsai (1995) method produced thresholds that (i) did not detect small bubbles, (ii) underestimated the size of bubbles detected or (iii) in some instances split a bubble in two different bubbles (Fig. 2b). In contrast, the thresholds produced by the CL-Otsu (HU = -273), and CL-Ridler (HU = -330), methods accurately identified bubbles in all images, including detecting very small bubbles, at the detection limit without introducing speckle in the segmented image (Fig. 2c); thresholds greater than -273 introduced noise in the results and thresholds lower than -500 underestimated both the number and the size of the bubbles. Therefore we proceeded by employing the thresholds generated by the CL-Otsu (HU = -273) and the CL-Ridler (HU = -330) algorithms as well as a threshold in between them (HU = -295) to compute the air volume fraction. Analysis of variance (ANOVA) demonstrated no significant differences between the values computed by the three selected thresholds ($p > 0.05$).

In the following paragraph, the air volume fraction is presented as the mean of the air volume fraction results computed using the three selected thresholds. The standard deviation about the mean air volume fraction computed from the three thresholds shows the potential range of the air volume fraction computed using these thresholds. The air volume fraction has to be clearly differentiated from the bulk ice total gas content (in mL L^{-1} ice). The bulk ice total gas content refers to the amount of O_2, N_2, and Ar, both (i) in dissolved phase in brine and (ii) in the gas phase in bubbles. Bulk ice total gas content is measured at larger spatial resolution (i.e. every 5 cm) compared

to the sub-millimetre resolution for data derived from X-ray tomography. In this work we use the terms "bubbles" and "air inclusions" interchangeably to denote gas phase inclusions in sea ice.

3 Results

3.1 Environmental conditions

The micrometeorological conditions at the Sea ice Environmental Research Facility (SERF) during the sea ice growth experiment during January 2013 are presented in detail by Rysgaard et al. (2014) and Galley et al. (2015b). In short, the ambient air temperature varied between −5 and −32 °C through the experiment from 13–26 January for an average of ∼ −22 °C; Snow thickness on the sea ice varied from 0 cm at the beginning of the experiment to maxima of 9 cm on 19 January and 8 cm on 26 January. Temporal variability in the snow thickness of course affected the sea ice temperature and therefore sea ice bulk salinity (Rysgaard et al., 2014).

3.2 Temperatures, salinity, brine volume fraction and bulk ice density

Sea ice temperature, bulk salinity, brine volume and bulk ice density profiles for cores sampled on 14 January (4 cm thick), 16 January, (8 cm thick) and 25 January (22 cm thick) are shown in Fig. 3 and Table 2.

On 14 January, the ice temperature ranged from −4.1 °C at the top to −1.7 °C at the bottom; its bulk salinity profile was approximately linear and ranged from 11 at the top to 25 at its base. This led to calculated brine volumes ranging linearly from top (11 %) to bottom (58 %). On 16 January, the ice temperature ranged from −8 °C at the top to −1.6 °C at the bottom; at this point the bulk ice salinity ranged from 2.2 to 10.3 and profile and was c-shaped. On 25 January, the bulk ice temperature ranged from −5.2 to −2 °C at the bottom and a c-shaped bulk salinity profile was observed ranging from 12.5 at the top to 1.3 in the middle and 8.5 in the bottom layer. On 16 and

Imaging air volume fraction in sea ice using non-destructive X-ray tomography

O. Crabeck et al.

Title Page

Abstract	Introduction
Conclusions	References
Tables	Figures

◄◄   ►►

◄   ►

Back   Close

Full Screen / Esc

Printer-friendly Version

Interactive Discussion

25 January, the calculated brine volume fraction profiles calculated were also c-shaped, with the minimum brine volume fraction occurring in the middle of each profile (2.2 % on 16 January and 1.3 % on 25 January).

Sea ice density profiles were computed for each of the three dates using the Mass–Volume technique. Bulk ice densities ranged from 0.84 ± 0.020 to $0.92 \pm 0.023\,\mathrm{Mg\,m^{-3}}$. The lowest densities were systematically found at the surface of the ice cover (Fig. 3).

3.3 Bulk ice total gas content and composition (O_2, N_2, Ar)

On all three ice core sampling dates, the observed bulk ice gas mixing ratios (mean values: $26.8\% \pm 2.8\ O_2$, $71.3\% \pm 3.2\ N_2$, and $1.8\% \pm 0.4$ Ar, Table 2) were intermediate to the atmospheric and dissolved in seawater values and total gas content ranged from $1.58\,\mathrm{mL\,L^{-1}}$ ice to $6.5\,\mathrm{mL\,L^{-1}}$ ice (Table 2).

As the ice thickened the total gas content increased from a mean of $1.58\,\mathrm{mL\,L^{-1}}$ on 14 January to a mean of $3.7\,\mathrm{mL\,L^{-1}}$ on 25 January. On 14 January, the bulk ice total gas content was $1.58\,\mathrm{mL\,L^{-1}}$. On 16 and 25 January, the bulk ice total gas content decreased linearly from a maximum in the sea ice surface layer of $4.72\,\mathrm{mL\,L^{-1}}$ ice and $6.5\,\mathrm{mL\,L^{-1}}$ to a minimum of 2.52 and $2.07\,\mathrm{mL\,L^{-1}}$ in the bottom of the ice core (Fig. 4). The bottom of each the ice cores (and the entire core on 14 January) was subsaturated ($SAT_f \leq 1$) (Fig. 4, Table 2). In contrast, the surface of the sea ice was supersaturated ($SAT_f > 1$) on 16 and 25 January. On 16 January, the bulk ice total gas content in the surface ice layer was 9.5 times higher than the theoretical equilibrium concentration ($SAT_f = 9.5$; Fig. 4, Table 2). On 25 January, the SAT_f reached 16 in the top layer of the ice.

3.4 Air porosity

3.4.1 Air volume fraction (V_a) derived from CT X-ray image analysis

The mean air volume fractions derived from the CT X-ray image data on 14 January, 16 and 25 were 0.59, 0.77 and 1.73 %, respectively. The maximum air volume observed in each core was 4.7 % on 14 January, 5.9 % on 16 January and 22.8 % on 25 January; that is, both the mean and maximum air volume fraction increased over time in the CT data. This can be visualized in the histograms of the Fig. 5, which shows the distribution of air volume fraction computed for every 0.6 mm thick slice of each core on the three sampling dates. For all three ice cores, the maximum air volume fraction was observed in the top 2 cm layer where the ice consisted of granular crystals (e.g. Fig. 6). In these granular layers, the brine volume exceeded systematically 5 % and the saturation factor was 9.5 on 16 January and reached 16 on 25 January (Fig. 6). As the granular ice layer thickened from 0.5 to 4 cm from 14 to 25 January, the air volume fraction in these layers increased. Below the granular ice layer, the crystal texture consisted of columnar ice on all three dates (Fig. 6). In the columnar zone, the air volume fraction was lower than 1 % on 14 and 16 January, and was lower than 2 % for 90 % of the columnar zone on 25 January (Fig. 6). In the columnar ice, we can distinguish the permeable ($V_b > 5$ %) and subsaturated ($SAT_f \leq 1$) ice in the bottom part, from the impermeable ($V_b < 5$ %) and supersaturated ($SAT_f > 1$) ice in the upper part (blue and white shaded regions respectively, in Fig. 7). At the transition between these two regions, we observed a slight increase of the air volume on 16 and 25 January. This vertical change can be visualized in the profiles (red shaded regions, in Fig. 7) and in the 3-D image in (Fig. 8).

3.4.2 Air inclusion morphology

The morphology of air inclusions is characterized quantitatively here using their diameters (Ø, mm). Most of the bubbles had diameters ≤ 1 mm; bubbles of this size were common at every depth interrogated by the CT imager (Fig. 9). Due to the non-destructive

nature of the CT X-ray method we were able to observe larger bubbles with diameters as large as 23.8 mm.

The bubble diameter ranged from 0.20 to 5.07 mm (14 January), from 0.21 to 7.55 mm (16 January) and 0.19 to 23.8 mm (25 January) (Fig. 9, Table 2). Between 14 and 25 January, the average bubble diameter increased from 0.72 to 1.73 mm. Both the mean and the maximum size increased over time.

In the entire image dataset encompassing the three dates, most of the observed bubbles in this work are micro bubbles (∅ ≤ 1 mm); micro bubbles represent 68.9 % of the bubble population derived by CT- X-ray imaging, large bubbles (1 mm < ∅ < 5 mm) represent 29.8 % of the bubble population and finally macro bubbles (∅ > 5 mm) represent 1.2 % (Fig. 9), however the proportion of micro, large and macro bubbles evolved over time. For 14 January, 82 % of the bubble population consisted of micro bubbles and less than 1 % of the bubble population were macro bubbles. On 16 January, 70.3 % of the bubble population were micro bubbles and 28,7 % large bubbles, and around 1 % consisted of macro bubbles. For 25 January, 37.2 % of the bubbles observed were micro bubbles, 58 % consisted of large bubbles, and 4.8 % of the bubbles were macro bubbles. Large bubbles occurred more frequently in the top of the ice core and macro bubbles with diameters larger than 5 mm were exclusively found close to the ice–atmosphere interface in the granular layer (Fig. 9a and b). Both the comparison of 2-D transversal slice and 3-D representations showed an accumulation of the number and size of bubbles in the top of the ice and over time (Figs. 8 and 9b).

4 Discussion

4.1 Computed tomography X-ray imaging as a non destructive method to compute the sea ice air volume fraction

Air volume fraction has been generally neglected in the physical characterization of sea ice properties because it is a small percentage of the total sea ice volume, and small

compared to the brine volume fraction. Although microstructural analysis of sea ice may produce reliable morphological results for air inclusions, thin sections only represent a small subsample of the ice core, are time consuming, can be operator-dependent, and the area and thickness of a thin section limit these studies to the interrogation of intact bubbles within a thin section. Density-derived air volume fraction results from the mass–volume technique generally have large errors and very low vertical resolution because they require large core subsample volumes (e.g. $5\,cm^3$).

By employing computed tomography X-ray imaging we provide high-resolution (sub-millimeter) profiles of the vertical distribution of air inclusions in sea ice, from which the sea ice air volume fraction can be accurately computed. Results of image analysis indicate that the air volume was $< 1\,\%$ in most of the ice, but systematically exceeded $5\,\%$ in the granular/snow ice top layer where an air volume fraction as high as $22.8\,\%$ was observed. X-ray tomography allows: (1) fast and accurate visualisation of the air inclusions, especially when compared to transmitted images, (2) extremely high resolution in three dimensions, (3) the ability to increase the size of the dataset compared to thin section microstructural analysis by imaging the whole core.

However, CT X-ray images (of porous materials in particular) are of such high resolution, use such large sample volumes and are so quick that traditional methodology can hardly be used to validate the imaged data at the same resolution. In order to validate the CT results, we computed the air volume fraction based on density measurements (Cox and Weeks, 1983) and compared it to the CT air volume fraction. The density ($M - V$) derived air volume profiles were generally slightly larger (Fig. 10a) but the two methods generally agree ($R^2 = 0.96$) (Fig. 10b). The standard deviation in air density-derived volume fraction (red bars in Fig. 10a) is larger than standard deviation from air CT-X-ray derived volume fraction. The CT air volume fraction also compared to the bulk ice total gas content ($mL\,L^{-1}$ ice) data derived from the GC analysis (Fig. 10c). The vertical gradients in the two datasets increased similarly from the bottom to the sea ice surface and both the total gas content ($mL\,L^{-1}$ ice) and the air volume fraction increased as the ice thickened over time. However, correlation between the air volume

fraction and the bulk ice gas content ($mL L^{-1}$ ice) (Fig. 10c) is not straightforward due in part to methodological constraints. The bulk ice total gas content measured by gas chromatography includes both the dissolved gases in the brine and the gas trapped in bubbles and cannot differentiate between them; the air volume fractions derived by X-ray tomography account for the air trapped in bubbles only. Further, the bulk ice total gas content from the GC were measured on different ice cores than the CT, which may have introduced variability. Further, the CT image voxels are sub-millimeter in size, whereas the bulk ice total gas concentration was measured on 5 cm sections of ice where some bubbles are inevitably cut in half when the core is destructively sampled so part of the gas is lost. This is further complicated by the fact that the probability of cutting a large bubble (with high gas content) is greater than for a small bubble with low gas content. Therefore the total gas content ($mL L^{-1}$ ice) data derived from the GC analysis is likely underestimated near the ice surface due to the cutting process. Further, gas within 5 cm thick sections may not be equally distributed; if thinner sections were analyzed the total gas content ($mL L^{-1}$ ice) values obtained may generate higher values in the top of the ice core similar to the CT image data ($\sim 20\,mL L^{-1}$ in the top most 2 cm and $\sim 4\,mL L^{-1}$ in the next 2 cm).

In the CT images, bubbles smaller than 0.25 mm appeared as mixed pixels leading to some underestimation of the air volume in the lower part of the ice core where most bubble diameters were < 1 mm. Our study is based on 633 ice slices of 0.6 mm thickness, which include 11 976 air inclusions. It is obvious that CT X-ray imaging clearly distinguishes between air inclusions and sea ice providing high-resolution sub-millimeter profiles of the air volume vertical distribution with better precision (mean standard deviation 0.69) linked almost entirely to the segmentation process and the resolution of the scanner.

Imaging air volume fraction in sea ice using non-destructive X-ray tomography

O. Crabeck et al.

Title Page

Abstract	Introduction
Conclusions	References
Tables	Figures

⏮   ⏭

◀   ▶

Back   Close

Full Screen / Esc

Printer-friendly Version

Interactive Discussion

4.2 Size of the air inclusion (i.e. bubbles): micro, large and macro air porosity

Previous studies of air inclusions morphology in sea ice were based on horizontal thin sections (e.g. Grenfell, 1983; Perovich and Gow, 1991, 1996; Cole et al., 2004; Light et al., 2003), restricting the information to inclusion cross-sections and unable to quantify the three dimensional nature of air inclusions. Grenfell (1983) measured bubble number distributions in small samples cut from first year sea ice, observing diameters ranging from 0.2 to 4 mm (e.g. radii 0.1 to 2 mm). Perovich and Gow (1996) reported mean bubble diameters ranging from 0.036 to 0.56 mm for 30 cm thick pancake ice and mean diameter of 2.6 mm on a multi-year hummock. Light et al. (2003) recorded 100 images from thin sections in transmitted light each with a 1.9 mm × 1.4 mm field of view. They reported bubble diameters between 0.008 to 0.14 mm in ice that was 175 cm thick (Light et al., 2003). We observed bubble diameters from 0.019 to 23.8 mm.

Most of the bubbles observed by CT X-ray imaging here are micro bubbles. Most of the air volume fractions observed are between 0 and 2 % (Fig. 11a); within this range the increasing number of bubbles produce a linear increase in the air volume fraction. To increase the air volume fraction over 2 %, the presence of large and macro bubbles are required. For lower bubble density (i.e. number of bubbles per mm^2), we observed higher air volume fraction while bubble size increases. While large and macro bubbles account for less than 18, 20 and 62 % of the bubble population observed for 14, 16 and 25 January respectively, the large and macro bubbles contribute systematically to more than 50 % of the total air volume fraction produced (Fig. 11b). While the air volume fraction consists of a mix of micro, large, and macro bubbles, the major parameter of control is most likely the size of the bubbles, rather than the number of bubbles (Fig. 11a and b). Micro bubbles are found at all depths in each ice core analyzed, but only have a significant influence on the air volume fraction when there is no large or macro bubbles (Fig. 11). For 14 January, the micro bubbles contributed for 48 % of the total air volume fraction because there were close to no macro bubbles (macro bubble = 0.059 % of total bubble population). In contrast macro bubbles were exclusively

found in the granular ice layers and more common on 25 January, where they contributed 58 % of total air volume fraction. Large bubbles contributed 52 and 60 % of the air volume fraction on 14 and 16 January. In addition, they were more prevalent when brine volume increased; when brine volume exceeded 5 %, around 50 to 70 % of the bubble population were large (Fig. 12b). Light et al. (2003) observed that bubbles were contained within brine and concluded that bubble size was limited by the size of the brine inclusion in which they resided. In several slices, we observed lighter pixels around air inclusions indicating these bubbles likely formed in a brine pocket. Brine density differs from ice density by only 20 %, so the medical CT-scanner employed here cannot unambiguously identify these pixels as brine inclusions. To visualize both air and brine inclusions in the same images, finer resolution with respect to sample density and finer spatial resolution are required of the imager. For example, Obbard et al. (2009) showed that micro-X-ray computed tomography with a voxel resolution of 15 μm is suitable for visualisation of brine and air inclusions.

4.3 Mechanism of air inclusions formation

Bulk salinity and bulk ice total gas content (mL L^{-1} ice) of sea ice is lower than in the seawater from which it formed, and that the bulk salinity profile and bulk ice total gas content of sea ice are seasonally dependent (Zhou et al., 2013). The bulk ice total gas content of sea ice was always lower than the value of 21.9 mL L^{-1} (23.8 mL kg^{-1}) expected for instant freezing seawater (Cox and Weeks, 1983). This is in agreement with previous reports that gases in seawater are preferentially expelled from growing ice, along with salts (Cox and Weeks, 1983, 1988; Killawee et al., 1998; Tison et al., 2002; Loose et al., 2009, 2011). The range of total gas content values for all the samples was 1.6 to 6.5 mL L^{-1}, which is in the lower end of ranges reported by Matsuo and Miyake (1966), Tison et al. (2002) and Crabeck et al. (2014b). Over time, the bulk ice total gas content increased from a mean of 1.6 mL L^{-1} ice to 3.7 mL L^{-1}, while the bulk salinity decreased from a mean of 17 (14 January) to 4.5 (25 January). It has been suggested that gas transport through sea ice occurs via processes separate from those control-

ling the transport of salt (Zhou et al., 2013). If the same processes were to regulate bulk ice salinity and bulk ice gas content, we would observe similar profiles and similar evolutions of these two parameters over time, but that is not the case. Rapid desalinisation occurred between 14 and 16 January, and the bulk salinity profile evolved to

5 a C-shaped profile over time (Fig. 3). In contrast, we observed a linear accumulation of gas content ($mL L^{-1}$) and air volume fraction from the base to the sea ice surface and an accumulation of gas content ($mL L^{-1}$) and air volume fraction within sea ice as it thickened over time. The transport of gases through sea ice is different than that of the solutes because gases may be present in the form of bubbles, instead of being

10 dissolved in the brine (Zhou et al., 2013).

In the multiphase sea ice system, the ratio between dissolved gas and bubbles depends on the bulk ice gas saturation state. In a closed system, when bubble nucleation is exclusively solubility driven, we should expect the air volume fraction to be a function of the saturation factor, which would lead to (i) a bubble-free layer in subsaturated sea

15 ice and (ii) high air volume fraction in supersaturated sea ice. The observed relationship between air volume fraction and saturation factor is not as straightforward (Fig. 12a).

Within (i) subsaturated sea ice (Fig. 12a and b, blue circles) the air volume fraction is independent of the brine volume fraction (Fig. 12a and b). In this case the air volume fraction never exceeded 2 and 50 % of the bubble diameters were < 1 mm (Fig. 12b).

20 These conditions ($V_a < 2$ %, $SAT_f \leq 1$, ⌀ < 1 mm) prevail on 14 January in the whole core (11.8 % < V_b < 58.6 %, Fig. 7), and near the permeable ice base for 16 and 25 January ($V_b \approx 20$ %, Fig. 7). When brine volume exceeds 5 % (Golden et al., 1998, 2007) and the Rayleigh (*Ra*) number increases (*Ra* systematically increased toward the sea ice bottom from 0 to 3, data not shown), previous studies indicate we can assume that

25 brine channels are connected in the vertical and able to exchange with the underlying seawater through gravity drainage in the brine system resulting in brine being replaced with underlying seawater through convection. As long as the brine is able to exchange with the underlying seawater the saturation factor is low and the gas species are therefore dissolved in the brine and can be rejected to the underlying water by convection.

This limits bubble formation, and hence the air volume fraction was $< 2\,\%$. Although the air volume fraction is low in these layers, it is somewhat surprising that the air volume fraction is > 0; in theory, bubble nucleation occurs when $SAT_f > 1$, so one might expect these subsaturated layers to be bubble-free. On 14 January, 98.8 % of the bubbles observed were located in subsaturated columnar sea ice and on 16 January and 25, 13 and 15 % (respectively) of the air inclusions observed were situated in subsaturated sea ice. Lubetkin (2003) observed bubble nucleation from saturated gas solutions at much lower saturations than expected from the theory. Bubble nucleation processes are favoured where (i) there are geometrical imperfections (Wilt, 1986), (ii) at "active sites" on a heterogeneous surface that can be chemically, structurally, or geometrically inhomogeneous (Deutscher and Fletcher, 1990; Kozisek et al., 2000); and (iii) by heterogeneous supersaturation away from thermodynamic equilibrium (Li and Yortsos, 1994), conditions which are all met in sea ice. Moreover, full-depth convection on 14 January and convection confined to the permeable bottom ice ($V_b \approx 20\,\%$) on 16 and 25 January likely produced local fluctuations in the amount of gas-saturated liquid. Convection-driven bubble nucleation in permeable sea ice has also been observed by Zhou et al. (2013). We suggest that brine drainage is only effective for the transport of dissolved gases to the underlying seawater if gas concentrations are close to the equilibrium concentration in the bottom permeable layer and in the absence of nucleation. Nucleation processes have the ability to increase the total gas content ($mL\,L^{-1}$ ice) of sea ice because once initiated, they ensure that gases will be maintained in the sea ice and not rejected to the underlying water (Tison et al., 2002). Convection driven nucleation processes likely produced micro bubbles in columnar permeable sea ice, which contributed to 12.1 % of the total air volume fraction observed.

Within (ii) supersaturated ice ($SAT_f > 1$), the air volume fraction and bubble size increased with brine volume, and the air volume fraction tended to be more likely a function of the saturation factor as the brine volume got larger (Fig. 12a and b). It appears that at low brine volumes, the air volume fraction is low regardless of the saturation factor (Fig. 12a). For brine volumes lower than 5 % the air volume fraction was $< 3\,\%$

and a majority of bubble diameters were $< 1\,mm$ (micro) (Fig. 12b). We observed supersaturated ice and low brine volumes ($V_b < 5\,\%$) in the middle of the ice cores on 16 and 25 January (white area in Fig. 7). On 16 and 25 January, 56 and 63 % of the bubbles were located in supersaturated columnar sea ice. Bubble nucleation is a function of both the brine volume as well as the saturation factor. Light et al. (2003) show that bubble nucleation create bubbles with diameters large enough that the surface tension is smaller than the internal tension of the brine, indicating some minimum brine channel size may be required to form a stablebubble. We observed a slight increase of air volume fraction at the transition between the subsaturated permeable sea ice and the supersaturated impermeable sea ice (at 60–70 % of the total sea ice thickness on 16 and 25 January). While convection driven nucleation occurs, in the whole bottom (few cm) convective layer, which is progressing downwards as the ice grows. Convective driven bubbles will naturally accumulate at the brine permeability transition. Bubbles are trapped when brine volume decrease below 5 %. Zhou et al. (2013) observed upward bubble migration at brine volumes $> 7\,\%$. On the contrary, it is only when the brine will be closing off below the brine volume threshold that the brine will start to supersaturate under cooling ($SAT_f = 2.7$ to 5) and eventually lead to solubility driven nucleation. We could expect that at any given time, a local air volume fraction maxima is located above the permeability transition.

Solubility-driven nucleation occurred in supersaturated columnar sea ice, and produced micro to large bubbles depending on the brine volume. It contributed to 22 % of the total observed air volume fraction.

We observed an accumulation of bubbles nearest the ice–atmosphere interface and generally within the ice surface granular ice layer (Figs. 6–8). This granular surface layer had the highest gas content, the highest saturation factor, the highest air volume fraction ($5\,\% < V_a < 22\,\%$) and contained macro bubbles with diameters as large as 5.1, 7.6, and 43.8 mm on 14, 16 and 25 January, respectively. The granular layer thickened from 0.5 to 4 cm between 14 and 25 January by surface processes linked to snow falls On the evening of 15 January, the first snowfall of the experiment covered the ice sur-

O. Crabeck et al.

face with 2 cm of snow, during which we observed wet snow ice and slush creation at the sea ice surface. Snowfalls and blowing snow between 18 and 19 January produced a snow layer as thick as 9 cm on the evening of 19 January, which was able to flood the ice by depressing it (negative free board). On 20 January, a slush layer (up to 3 cm thick) was observed at the snow base. The wet snow and seawater at the ice surface eventually froze, contributing to the thickening of the granular layer at the surface by forming snow and superimposed ice. As the granular layer thickened, the air volume fraction nearest the ice interface increased as well. The increase of air volume fraction and gas content (mL L^{-1} ice) in this granular layer can be explained by the combination of several processes. The formation of granular/snow ice is well known to contain more gas than columnar ice because it traps gas directly from the atmosphere (Tsurikov, 1979; Cole et al., 2004; Zhou et al., 2013). In this layer, the brine volume exceeded 10 % on 16 and 25 January, and SAT$_f$ was > 9 on 16 January and > 10 on 25 January, a combination that allowed large bubbles to form. We systemically observed an increase of the bubble size and a decrease of the bubble density in the granular ice (Fig. 11a), suggesting the presence of coalescence processes, which we can clearly show using X-ray images (Fig. 13). A succession of 0.6 mm thick transversal slices at 2.46 cm depth from 25 January is shown in Fig. 13. In the first slice, we identify 4 individual bubbles, which coalesce into a single bubble. The rapid freezing of slush and wet snow forces gas out of solution, building up the air volume fraction nearest the ice–atmosphere interface. We link the presence of macro bubbles and coalescence to the rapid freezing of slush and wet snow at the ice interface, and indicate that snow and snowfall play an important role in the gas dynamics of new and young sea ice (amongst their myriad of other physical effects). While bubbles resulting of granular/snow ice formation accounted for 20 % of the bubble population observed, the porosity produced by frazil formation accounted for 66 % of the total porosity recorded.

The presence of large bubbles and air volume fraction > 5 % in the top of the ice cover should potentially mediate gas fluxes over sea ice. Kotovich et al. (2015) illustrate that

bubbles migrating upward out of the ice contribute to 80 % of the CO_2 fluxes from sea ice to the atmosphere during ice growth in a model study.

5   Conclusions and perspectives

We used computed tomography X-ray imaging to quantify air inclusion distribution in sea ice, from which we derive the air volume fraction. Air inclusions are quickly and easily identified by X-ray tomography and quantitatively analyzed using segmentation techniques. The threshold selection is a crucial step requiring careful examination to provide successful results. The results from the CT X-ray analysis showed similar trends to conventional density and bulk ice total gas content ($mL L^{-1}$ ice) measurement methods. X-ray imaging is non-destructive and allows for a direct determination of air inclusions in sea ice at high resolution with low errors and creates large datasets very quickly.

We differentiate between micro bubbles, large bubbles and macro bubbles diameters. Micro bubbles are found both in the bottom permeable layers ($V_b > 5$ %) and in the intermediate impermeable layers ($V_b < 5$ %) as well as in surface layers. Large bubbles are found more frequently where brine volume exceeded 5 % and macro bubbles occur exclusively in the granular snow ice layer nearest the ice–atmosphere interface. Micro bubbles are the most abundant type of bubbles observed, they only accounted for 15 % of the total air volume fraction recorded. In contrast, macro bubbles linked to granular snow ice layer accounted for less than 2 % of the total bubbles but their size (volume) accounts for 66 % of the total air volume fraction of the sea ice imaged. While the air volume fraction results from a mix of micro, large and macro bubbles, the factor controlling the air volume fraction is most likely the size of the air inclusions (i.e. bubbles) (Table 3).

We suggest that bubbles observed in the subsaturated permeable layers are formed by convection-driven nucleation. Here the amount and size of the bubbles are limited by the low saturation state of the brine. Bubbles observed in impermeable supersaturated

Title Page

Abstract | Introduction

Conclusions | References

Tables | Figures

|◄ | ►|

◄ | ►

Back | Close

Full Screen / Esc

Printer-friendly Version

Interactive Discussion

sea ice are formed by solubility-driven nucleation, where the amount and bubble size is limited by the amount of brine (i.e. size of the brine inclusions). At any growth step, a local maximum exists in the vertical just above the permeability transition, confirming the important role of this transition zone in shaping the vertical air volume fraction distribution. Macro bubbles located in the near-surface sea ice are linked to the presence of granular ice and the formation of snow ice (Table 3).

We conclude that processes regulating the vertical distribution of salts do not control the vertical distribution of gases, because most of the total gas content ($mL L^{-1}$ ice) exists as bubbles rather than being dissolved in the brine as previously argued (Tison et al., 2002; Zhou et al., 2013; Moreau et al., 2014; Crabeck et 2014a, b). Once micro and/or macro bubbles form they are segregated from the transport pathway of dissolved salts, because bubbles will not drain out of the ice by convection due to their low density, so nucleation leads to an accumulation of gas in sea ice. Our work provides the first detailed visual demonstration and quantification of these processes.

As a result of the presence of large bubbles and higher air volume fraction measurements in sea ice we introduce new perspectives on processes regulating gas exchange at the ice–atmosphere interface, and note that the air volume fraction should be an important inclusion in parameterizations of sea ice permeability. CT X-ray imaging may allow for visualizations of transport pathways, for example the upward migration of bubbles. CT X-ray imaging could be used to investigate the effect of different thermal and crystal texture regimes on bubble formation, dimensions, and their vertical and horizontal distribution in a large number of replicate cores from the same ice cover. This information is vital to the improvement of models involving transport of biochemical compounds and gas transfer between the ocean and the atmosphere in polar oceans.

Imaging air volume fraction in sea ice using non-destructive X-ray tomography

O. Crabeck et al.

Title Page

Abstract	Introduction
Conclusions	References
Tables	Figures

Back | Close

Full Screen / Esc

Printer-friendly Version

Interactive Discussion

References

Bennington, K. O.: Desalination features in natural sea ice, J. Glaciol., 6, 845–857, 1967.

Bock, C. and Eicken, H.: A magnetic resonance study of temperature-dependent microstructural evolution and self-diffusion of water in Arctic first-year sea ice, Ann. Glaciol., 40, 179–184, 2005.

Boespflug, X., Ross, N., Long, B., and Dumais, J. F.: Axial tomodensitometry: correlation between tomographic intensity and density of materials, Can. J. Earth Sci., 31, 426–434, 1994.

Carte, A. E.: Air bubbles in ice, P. Phys. Soc., 77, 757–768, 1961.

Cole, D. M. and Shapiro, L. H.: Observations of brine drainage networks and microstructure of first-year sea ice, J. Geophys. Res., 103, 21739–21750, 1998.

Cox, G. F. N. and Weeks, W. F.: Brine Drainage and Initial Salt Entrapment in Sodium Chloride Ice, Cold Regions Research and Engineering Laboratory Research Report 345, Cold Regions Research and Engineering Laboratory, Hanover, NH, 1975.

Cox, G. F. N. and Weeks, W. F.: Equations for determining the gas and brine volumes in sea-ice samples, J. Glaciol., 29, 306–316, 1983.

Crabeck, O., Delille, B., Else, B., Thomas, D. N., Geilfus, N. X., Rysgaard, S., and Tison, J. L.: First "in situ" determination of gas transport coefficients (DO_2, DAr, and DN_2) from bulk gas concentration measurements (O_2, N_2, Ar) in natural sea ice, J. Geophys. Res.-Oceans, 119, 6655–6668, doi:10.1002/2014JC009849, 2014a.

Crabeck, O., Delille, B., Thomas, D., Geilfus, N.-X., Rysgaard, S., and Tison, J.-L.: CO_2 and CH_4 in sea ice from a subarctic fjord under influence of riverine input, Biogeosciences, 11, 6525–6538, doi:10.5194/bg-11-6525-2014, 2014b.

Delille, B., Vancoppenolle, M., Geilfus, N.-X., Tilbrook, B., Lannuzel, D., Schoemann, V., Becquevort, S., Carnat, G., Delille, D., Lancelot, C., Chou, L., Dieckmann, G. S., and Tison, J.-L.: Southern Ocean CO_2 sink: The contribution of the sea ice, J. Geophys. Res.-Oceans, 119, 6340–6355, doi:10.1002/2014JC009941, 2014.

Duliu, O. G.: Computer axial tomography in geosciences: an overview, Earth-Sci. Rev., 48, 265–281, 1999.

Eicken, H., Bock, C., Wittig, R., Miller, H., and Poertner, H.-O.: Magnetic resonance imaging of sea-ice pore fluids: methods and thermal evolution of pore microstructure, Cold Reg. Sci. Technol., 31, 207–225, 2000.

Eide, L. I. and Martin, S.: The formation of brine drainage features in young sea ice, J. Glaciol., 14, 137–154, 1975.

Feltham, D. L., Untersteiner, N., Wettlaufer, J. S., and Worster, M. G.: Sea ice is a mushy layer, Geophys. Res. Lett., 33, L14501, doi:10.1029/2006GL026290, 2006.

Fritsen, C. H., Lytle, V. I., Ackley, S. F., and Sullivan, C. W.: Autumn bloom of Antarctic pack-ice algae, Science, 266, 782–784, 1994.

Galley, R. J., Else, B. G. T., Geilfus, N.-X., Hare, A. A., Isleifson, D., Barber, D. G., and Rysgaard, S.: Imaged brine inclusion in young sea ice – Shape, distribution and formation timing, Cold Reg. Sci. Technol., 111, 39–48, doi:10.1016/j.coldregions.2014.12.011, 2015a.

Galley, R. J., Else, B. G. T., Geilfus, N.-X., Hare, A. A., Babb, D., Papakyriakou, T., Barber, D. G., and Rysgaard, S.: Micrometeorological control of frost flower growth and decay on young sea ice, Arctic, 68, 79–92, doi:10.14430/arctic4457, 2015b.

Garcia, H. E. and Gordon, L. I.: Oxygen solubility in seawater: better fitting equations, Limnol. Oceanogr., 37, 1307–1312, 1992.

Geilfus, N.-X., Tison, J.-L., Ackley, S. F., Galley, R. J., Rysgaard, S., Miller, L. A., and Delille, B.: Sea ice $p$$CO_2$ dynamics and air–ice CO_2 fluxes during the Sea Ice Mass Balance in the Antarctic (SIMBA) experiment – Bellingshausen Sea, Antarctica, The Cryosphere, 8, 2395–2407, doi:10.5194/tc-8-2395-2014, 2014.

Geilfus, N.-X., Galley, R. J., Crabeck, O., Papakyriakou, T., Landy, J., Tison, J.-L., and Rysgaard, S.: Inorganic carbon dynamics of melt-pond-covered first-year sea ice in the Canadian Arctic, Biogeosciences, 12, 2047–2061, doi:10.5194/bg-12-2047-2015, 2015.

Title Page

Abstract | Introduction

Conclusions | References

Tables | Figures

◄ | ►

◄ | ►

Back | Close

Full Screen / Esc

Printer-friendly Version

Interactive Discussion

Golden, K. M., Ackley, S. F., and Lytle, V. I.: The percolation phase transition in sea ice, Science, 282, 2238–2241, 1998.

Golden, K. M., Eicken, H., Heaton, A. L., Miner, J., Pringle, D. J., and Zhu, J.: Thermal evolution of permeability and microstructure in sea ice, Geophys. Res. Lett., 34, L16501, doi:10.1029/2007GL030447, 2007.

Grenfell, T. C.: A theoretical model of the optical properties of sea ice in the visible and near infrared, J. Geophys. Res., 88, 9723–9735, 1983.

Hamme, R. C. and Emerson, S. R.: The solubility of neon, nitrogen and argon in distilled water and seawater, Deep-Sea Res. Pt. I, 51, 1517–1528, 2004.

Hare, A. A., Wang, F., Barber, D., Geilfus, N.-X., Galley, R. J., and Rysgaard, S.: pH evolution in sea ice grown at an outdoor experimental facility, Mar. Chem., 154, 46–54, doi:10.1016/j.marchem.2013.04.007, 2013.

Hounsfield, G. N.: Computerized transverse axial scanning (tomography), Part 1: Description of system, Brit. J. Radiol., 46, 1016–22, 1973.

Hunter, M. W., Dykstra, R., Lim, M. H., Haskell, T. G., and Callaghan, P. T.: Using Earth's field NMR to study brine content in Antarctic sea ice: Comparison with salinity and temperature estimates, Appl. Magn. Reson., 36, 1–8, doi:10.1007/s00723-009-0003-9, 2009.

Iassonov, P., Gebrenegus, T., and Tuller, M.: Segmentation of X-ray computed tomography images of porous materials: a crucial step for characterization and quantitative analysis of pore structures, Water Resour. Res., 45, W09415, doi:10.1029/2009WR008087, 2009.

Jones, S. F., Evans, G. M., and Galvin, K. P.: Bubble nucleation from gas cavities – a review, Adv. Colloid Interfac., 80, 27–50, 1999.

Kapur, J. N., Sahoo, P. K., and Wong, A. K. C.: A new method for gray-level picture thresholding using the entropy of the histogram, Graph. Model. Im. Proc., 29, 273–285, doi:10.1016/0734-189X(85)90125-2, 1985.

Killawee, J. A., Fairchild, I. J., Tison, J. L., Janssens, L., and Lorrain, R.: Segregation of solutes and gases in experimental freezing of dilute solutions: implications for natural glacial systems, Geochim. Cosmochim. Acta, 62, 3637–3655, 1998.

Knoll, G. F.: Radiation Detection and Measurment, John Wiley & Sons, New York, 1989.

Kotovitch, M., Moreau, S., Zhou, J., Vancoppenolle, M., Dieckmann, G. S., Evers, K.-U., Van der Linden, F., Thomas, D. N., Tison, J.-L., and Delille, B.: Measurements of air–ice CO_2 fluxes over experimental sea ice emphasize the role of bubbles in gas transport during ice growth, J. Elementa, submitted, 2015.

Title Page

Abstract | Introduction

Conclusions | References

Tables | Figures

|◄ | ►|

◄ | ►

Back | Close

Full Screen / Esc

Printer-friendly Version

Interactive Discussion

Krembs, C., Gradinger, R., and Spindler, M.: Implications of brine channel geometry and sur-face area for the interaction of sympagic organisms in Arctic sea ice, J. Exp. Mar. Biol. Ecol., 243, 55–80, 2000.

Langway, C. C.: Ice Fabrics and the Universal Stage, rep. 62, US Snow, Ice and 496 Permafrost Research Establishment, Wilmette, IL, 1958.

Lepparanta, M. and Manninen, T.: The Brine and Gas Content of Sea Ice with Attention to Low Salinities and High Temperatures, report 2, Finnish Institute of Marine Research, Helsinki, Finland, 15 pp., 1988.

Light, B., Maykut, G. A., and Grenfell, T. C.: Effects of temperature on the microstructure of first-year Arctic sea ice, J. Geophys. Res., 108, 3051, doi:10.1029/2001JC000887, 2003.

Loose, B., McGillis, W. R., Schlosser, P., Perovich, D., and Takahashi, T.: Effects of freezing, growth, and ice cover on gas transport processes in laboratory seawater experiments, Geo-phys. Res. Lett., 36, L05603, doi:10.1029/2008gl036318, 2009.

Loose, B., Schlosser, P., Perovich, D., Ringelberg, D., Ho, D. T., Takahashi, T., Richter-Menge, J., Reynolds, C. M., McGillis, W. R., and Tison, J. L.: Gas diffusion through columnar laboratory sea ice: implications for mixed-layer ventilation of CO_2 in the seasonal ice zone, Tellus B, 63, 23–39, doi:10.1111/j.1600-0889.2010.00506.x, 2011.

Lubetkin, S. D.: Why is it much easier to nucleate gas bubbles than theory predicts?, Langmuir, 19, 2575–2587, 2003.

Matsuo, S. and Miyake, Y.: Gas composition in ice samples from Antarctica, J. Geophys. Res., 71, 5235–5241, 1966.

Moreau, S., Vancoppenolle, M., Zhou, J., Tison, J.-L., Delille, B., and Goosse, H.: Modelling argon dynamics in first-year sea ice, Ocean Model., 73, 1–18, 2014.

Nomura, D., Yoshikawa-Inoue, H., and Toyota, T.: The effect of sea-ice growth on air–sea CO_2 flux in a tank experiment, Tellus B, 58, 418–426, 2006.

Nomura, D., Yoshikawa-Inoue, H., Toyota, T., and Shirasawa. K.: Effects of snow, snow-melting and re-freezing processes on air–sea ice CO_2 flux, J. Glaciol., 56, 262–270, 2010.

Notz, D. and Worster. M. G.: In situ measurements of the evolution of young sea ice, J. Geophys. Res., 113, C03001, doi:10.1029/2007JC004333, 2008.

Obbard, R., Troderman, G., and Baker, I.: Imaging brine and air inclusions in sea ice using micro-X-ray computed tomography, correspondance, J. Glaciol., 55, 1113–1115, 2009.

Otsu, N.: A threshold selection method from gray-level histograms, IEEE T. Syst. Man Cyb., 9, 62–66, doi:10.1109/TSMC.1979.4310076, 1979.

Imaging air volume fraction in sea ice using non-destructive X-ray tomography

O. Crabeck et al.

Title Page

Abstract	Introduction
Conclusions	References
Tables	Figures

|◄ | ►|

◄ | ►

Back | Close

Full Screen / Esc

Printer-friendly Version

Interactive Discussion

Pal, N. R.: Minimum cross entropy threshold selection, Pattern Recogn., 29, 575–580, doi:10.1016/0031-3203(95)00111-5, 1996.

Pal, N. R. and Pal, S. K.: Entropic thresholding, Signal Process., 16, 97–108, doi:10.1016/0165-1684(89)90090-X, 1989.

5 Papakyriakou, T. and Miller, L.: Springtime CO_2 exchange over seasonal sea ice in the Canadian Arctic Archipelago, Ann. Glaciol., 52, 215–224, 2011.

Perovich, D. K. and Gow, A. J.: A quantitative description of sea ice inclusions, J. Geophys. Res.-Oceans, 101, 18327–18343, 1996.

Pringle, D. J., Miner, J. E., Eicken, H., and Golden, K. M.: Pore space percolation in sea ice
10 single crystals, J. Geophys. Res., 114, C12017, doi:10.1029/2008JC005145, 2009.

Raynaud, D., Delmas, R., Ascencio, M., and Legrand, M.: Gas extraction from polar ice cores: a critical issue for studying the evolution of atmospheric CO_2 and ice-sheet surface elevation, Ann. Glaciol., 3, 265–268, 1982.

Rees Jones, D. W. and Worster, M. G.: A simple dynamical model for gravity drainage of brine
15 from growing sea ice, Geophys. Res. Lett., 40, 1–5, doi:10.1029/2012GL054301, 2013.

Ridler, T. W. and Calvard, S.: Picture thresholding using an iterative selection method, IEEE T. Syst. Man Cyb., 8, 630–632, 1978.

Rosin, P. L.: Unimodal thresholding, Pattern Recogn., 34, 2083–2096, doi:10.1016/S0031-3203(00)00136-9,1978, 2001.

20 Rysgaard, S., Wang, F., Galley, R. J., Grimm, R., Notz, D., Lemes, M., Geilfus, N.-X., Chaulk, A., Hare, A. A., Crabeck, O., Else, B. G. T., Campbell, K., Sørensen, L. L., Sievers, J., and Papakyriakou, T.: Temporal dynamics of ikaite in experimental sea ice, The Cryosphere, 8, 1469–1478, doi:10.5194/tc-8-1469-2014, 2014.

Semiletov, I. P., Makshtas, A., Akasofu, S. I., and Andreas, E. L.: Atmospheric CO_2 balance: the
25 role of Arctic sea ice, Geophys. Res. Lett., 31, L05121, doi:10.1029/2003GL017996, 2004.

Sezgin, M. and Sankur. B.: Survey over image thresholding techniques and quantitative performance evaluation, J. Electron. Imaging, 13, 146–165, doi:10.1117/1.1631315, 2004.

Shannon, C. E. and Weaver, W.: The mathematical theory of communication, Bell Syst. Tech. J., 27, 379–423,1948.

30 Skoog, D. A., West, D. M., and Holler, F. J.: Chimie Analytique, De Boeck Univ., Paris, 1997.

Stefels, J., Carnat, G., Dacey, J. W. H., Goossens, T., Elzenga, J. T. M., and Tison, J. L.: The analysis of dimethylsulfide and dimethylsulfoniopropionate in sea ice: dry-crushing and melting using stableisotope additions, Mar. Chem., 128–129, 34–43, 2012.

Title Page

Abstract | Introduction

Conclusions | References

Tables | Figures

|◄ | ►|

◄ | ►

Back | Close

Full Screen / Esc

Printer-friendly Version

Interactive Discussion

Sund, R. and Eilertsen. K.: An algorithm for fast adaptive image binarization with applications in radiotherapy imaging, IEEE T. Med. Imaging, 22, 22–28, doi:10.1109/TMI.2002.806431, 2003.

Timco, G. W. and Frederking. R. M. W.: A review of sea ice density, Cold Reg. Sci. Technol., 24, 1–6, 1996.

Tison, J. L., Haas, C., Gowing, M. M., Sleewaegen, S., and Bernard, A.: Tank study of physico-chemical controls on gas content and composition during growth of young sea ice, J. Glaciol., 48, 177–191, 2002.

Tsai, D. M.: A fast thresholding selection procedure for multimodal and unimodal histograms, Pattern Recogn. Lett., 16, 653–666, doi:10.1016/0167-8655(95)80011-H, 1995.

Tsurikov, V.: The formation and composition of the gas content of sea ice, J. Glaciol., 22, 67–81, 1979.

UNESCO: Eight Report of the Joint Panel on Oceanographic Tables and Standards, UNESCO Tech. Pap. Mar. Sci., Paris, France, 28 pp., 1978.

Vancoppenolle, M., Meiners, K. M., Michel, C., Bopp, L., Brabant, F., Carnat, G., Delille, .B, Lannuzel, D., Madec, G., Moreau, S., Tison, J.-L., and van der Merwe, P.: Role of sea ice in global biogeochemical cycles: emerging views and challenges, Quaternary Sci. Rev., 79, 207–230, doi:10.1016/j.quascirev.2013.04.011, 2013.

Worster, M. G.: The dynamics of mushy layers, in: Interactive Dynamics of Convection and Solidification, NATO ASI Ser. E219, Kluwer, Dordrecht, 113–138, 1992.

Worster, M. G.: Convection in mushy layers, Annu. Rev. Fluid Mech., 29, 91–122, 1997.

Yen, J.-C., Chang, F. J., and Chang, S.: A new criterion for automatic multilevel thresholding, IEEE T. Image Process., 4, 370–378, doi:10.1109/83.366472, 1995.

Zack, G. W., Rogers, W. E., and Latt, S. A.: Automatic measurement of a sister chromatid exchange frequency, J. Histochem. Cytochem., 25, 741–753, 1997.

Zemmelink, H. J., Delille, B., Tison, J. L., Hintsa, E. J., Houghton, L., and Dacey, J. W. H.: CO_2 deposition over the multi-year ice of the western Weddell Sea, Geophys. Res. Lett., 33, L13606, doi:10.1029/2006GL026320, 2006.

Zhou, J. Y., Delille, B., Eicken, H., Vancoppenolle, M., Brabant, F., Carnat, G., Geilfus, N. X., Papakyriakou, T., Heinesch, B., and Tison, J. L.: Physical and biogeochemical properties in landfast sea ice (Barrow, Alaska): insights on brine and gas dynamics across seasons, J. Geophys. Res.-Oceans, 118, 3172–3189, doi:10.1002/jgrc.20232, 2013.

Title Page

Abstract | Introduction

Conclusions | References

Tables | Figures

|◄ | ►|

◄ | ►

Back | Close

Full Screen / Esc

Printer-friendly Version

Interactive Discussion

Table 1. Comparison of measured air porosity in function of segmentation methods for 25 January.

Method	Threshold	Mean V_a (%)	Max V_a (%)	Min V_a (%)
EN Yen	−190	3	27	0.42
EN Kapur	−210	2.7	25	0.22
HS Zack	−500	0.85	10	0.08
HS-tsai	−659	0.32	8	0.03
CL-Otsu	−273	1.8	24	0.11
CL-Ridler	−659	1.7	22	0.11

Table 2. Resumes the main sea ice characteristic and sea ice properties.

Data		14 Jan	16 Jan	25 Jan
Ice thickness (cm)		4	8	22
Temperature (C°)		−4.1–1.7	−8.4–1.6	−5.2–2.1
Salinity		11.4–25.8	2.26–10.3	1.3–12.5
Brine volume fraction (%) (V_b, liquid porosity)		11.8–58.6	2.26–20.4	1.3–20.6
Bulk ice Density ($Mg\,m^{-3}$)		0.91	0.89–0.92	0.84–0.92
Air volume fraction (%) (V_a, air porosity data derivate from CT X-ray)		0.15–4.93	0.21–5.69	0.12–22.8
Air inclusions diameter (mm)		0.20–5.07	0.21–7.55	0.19–23.8
Gas composition (mixing ratio)	O_2 %	23.7	29.4	27.1
	Ar %	1.4	2.2	1.96
	N_2 %	74.9	68.4	70.8
Bulk ice gas concentration ($\mu mol\,L^{-1}$ ice, Data derivate from GC)	O_2	16.7	34.7–63.6	15.2–70.6
	Ar	0.91	2.8–5.7	0.98–6.8
	N_2	49	83.7–141.4	42.5–192.7
Buk ice total gas content ($mL\,L^{-1}$ ice, $O_2 + Ar + N_2$)		1.58	2.5–4.7	2–6.5
Gas Saturation factor (SAT_f)		0.82 (bottom)	9.5 (top)–1.1 (bottom)	16 (top)–0.9

Table 3. Synthesizes the classification of the air inclusions **(a)** and the main parameters influencing the air volume fraction **(b)**. The abundance is defined as the percentile of inclusions concerned by the class or the processes listed in column one, (100 % is the total of inclusions observed in the three data set – 14 January + 16 January + 25 January). The importance is the percentile of the porosity produced by the class or processes listed in column one (100 % is the total of air volume fraction observed in the three data set – 14 January + 16 January + 25 January).

(a)	Air inclusion Classification	Abundance (% of the total air inclusions observed)	Importance (% of the air volume fraction produced)	Location	
	Micro	68.9 %	15 %	Columnar and Granular	
	Large	29.8 %	65 %	Columnar and Granular Depend most likely of V_b	
	Macro	1.3 %	20 %	Granular/snow icel	
(b)	Nucleation Processes	Limitation factor	Abundance	Importance	Type of air inclusions produced	Location
	Convection driven	Saturation level	25 %	12 %	Most likely micro	subsaturated columnar
	Solubility Driven	Brine volume fraction	54 %	22 %	Micro to large	Supersaturated Columnar
	Snow ice formation		21 %	66 %	Micro Large Macro	Granular/snow ice

Title Page

Abstract | Introduction

Conclusions | References

Tables | Figures

|◄ | ►|

◄ | ►

Back | Close

Full Screen / Esc

Printer-friendly Version

Interactive Discussion
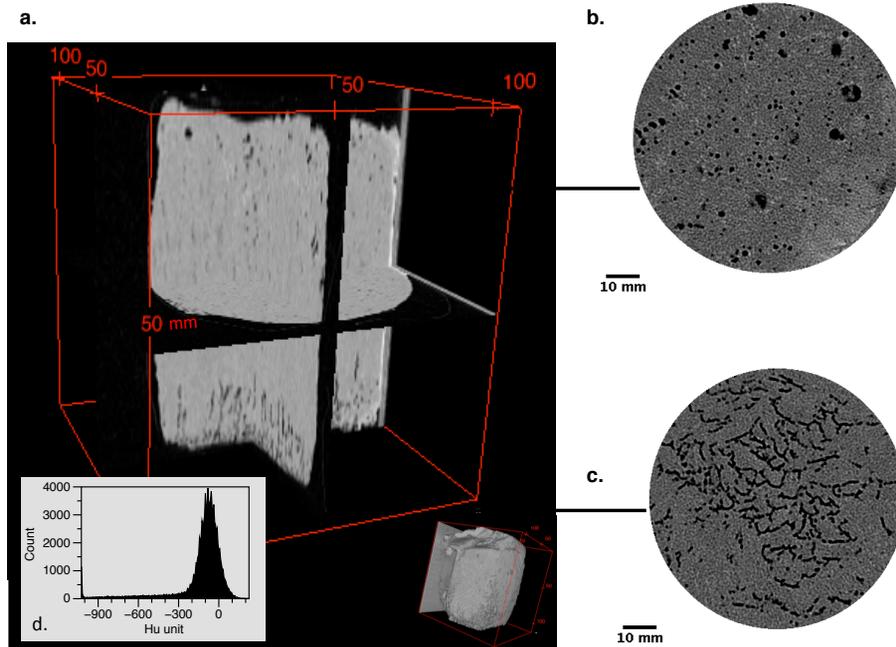
Figure 1. (a) 3-D orthoslice view from raw images of 16 January, consisting of two longitudinal slices and transversal slices, lighter grey represent the ice matrices and black area represent the air inclusions (i.e. bubbles); **(b)** top transversal slice at 0.65 mm depth, every black dots represent an air inclusion (i.e. bubbles); **(c)** bottom transversal slice at 8 cm depth, all the black dots show drained brine; **(d)** histogram of HU unit (Ct value) recoded for 186 transversal slices of 0.6 mm thick for 16 January.

a. **Raw image**

EN-Kapur HU-value = -210

EN-Yen HU-value = -190

10 mm

10 mm

10 mm

Nbr bubble: 732
V_a=12.59%

Speckle : 76% of the bubbles < pixel size.

Speckle : 62% of the bubbles < pixel size.

b.

10 mm

10 mm

10 mm

Nbr bubble: 96
V_a= 6.8%

1.Micro bubbles missing , 2. underestimation of size ; bubble diameter : 0.45mm, 3. Single bubble split into two individual inclusions.

c.

10 mm

10 mm

10 mm

Nbr bubble 173
V_a=8.73%

Nbr bubble 125, V_a=7.8%

1.Detect micro bubbles; 2. right size; bubble radii : 0.86 mm; 3. single bubble.

d.

HU-value

0

−500

−1000

0   20   40   60

Distance (mm) crossectional section)

- Hu-value
- Yen (HU-value -190)
- Otsu (HU-value -273)
- Ridler (HU-value-330)
- Tsai (HU-value -659)
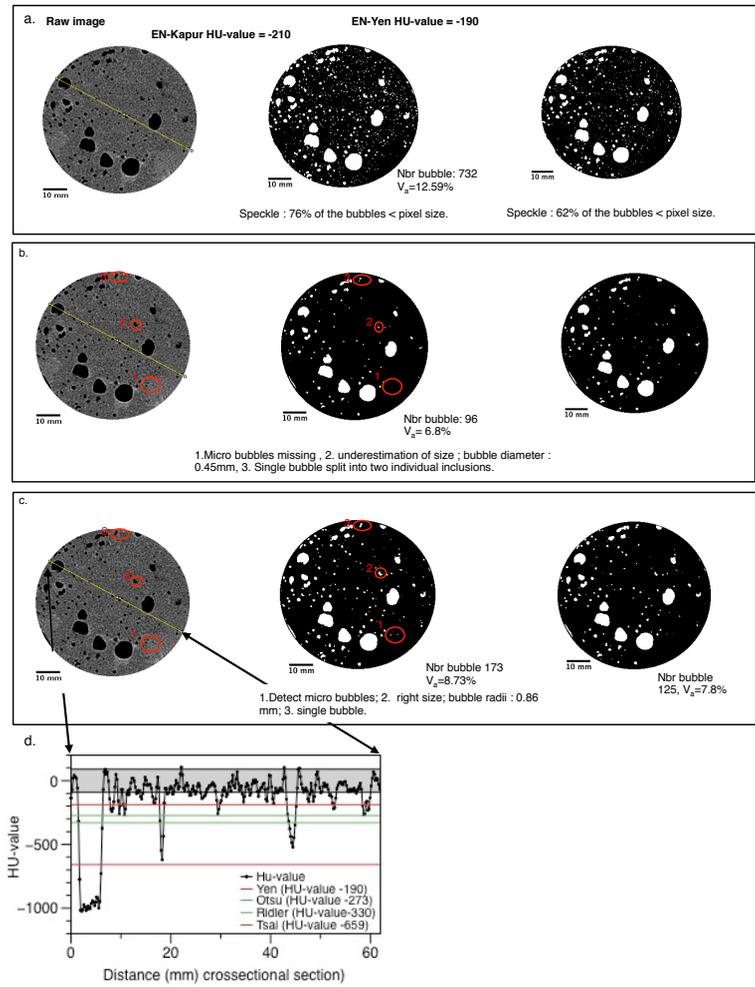
Figure 2. Panel **(a)** show successively a raw transversal slice where grey pixels represents ice and black pixels represents air, and two binarized images using a HU Value of -190 and of -210 as threshold selected by the EN-yen and the EN-Kapur algorithm respectively. The withe pixels are the air-selected pixel. **(b)** and **(c)** show successively the same raw and binarized image but using for **(b)** a HU value of -500 and of -659 as threshold selected by the HS-Zack and HS-Tsay algorithm and for **(c)** a HU value of -273 and of -330 as threshold selected by the CL-Otsu and Cl-Ridler algorithm. **(d)** shows the distribution of HU value along the transect (yellow line in panel **a**, **b** and **c**), the successive solid lines represents the different thresholds, green effective, red ineffective thresholds.
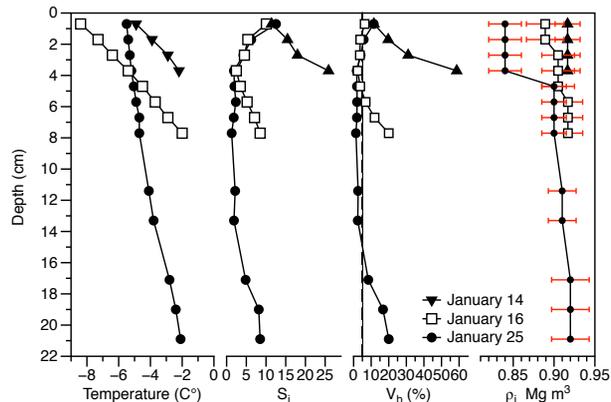
Figure 3. Shows bulk ice in situ temperature ($^\circ$C), bulk ice salinity, brine volume fraction (V_b, %), the dotted line is a reference value for the permeability threshold following Golden et al. (1998, 2007) and the bulk ice density (ρ_i, Mg m^{-3}), the red bars show the standard deviation of the mean of the results linked to imperfect volume dimension.
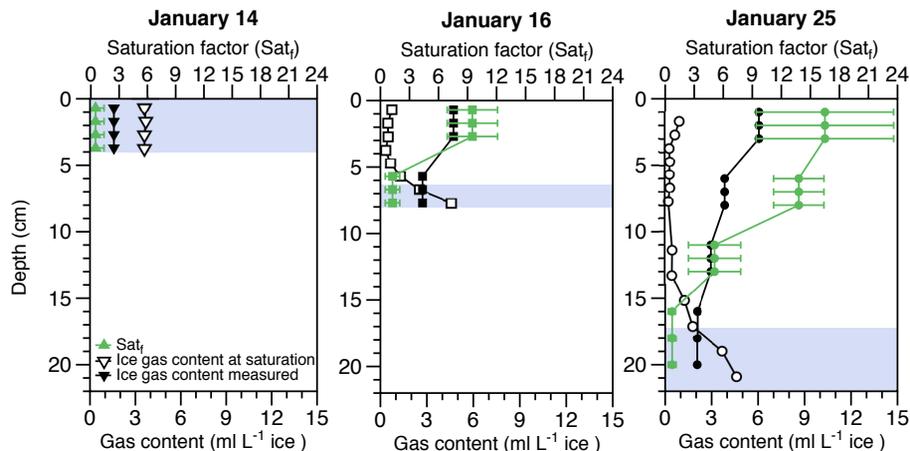
Figure 4. Shows the evolution of the total gas content in bulk sea ice measured by gas chromatography as the sum O_2, N_2, Ar and compared (i) to the theoretical bulk ice gas content at atmospheric saturation in white and (ii) to the saturation factor in green, the blue area underlines the subsaturated sea ice ($SAT_f \leq 1$) which is t he part of the ice where the gas content is under or close to the theoretical concentration at atmospheric concentration. The SAT_f is the ratio of observed concentration in bulk ice ($C_{bulk\ ice}$) and the theoretical saturation concentration in bulk ice ($C_{saturation}$). $C_{bulk\ ice}$ is measured on 5 cm ice cube while $C_{saturation}$ is computed at a thinner scale, for a same measure of $C_{bulk\ ice}$, we can compute several potential SAT_f, we present the mean SAT_f and it is standard deviation per 5 cm of ice. The standard deviation is larger while we have a strong gradient of temperature, salinity and brine volume along 5 cm piece of ice.
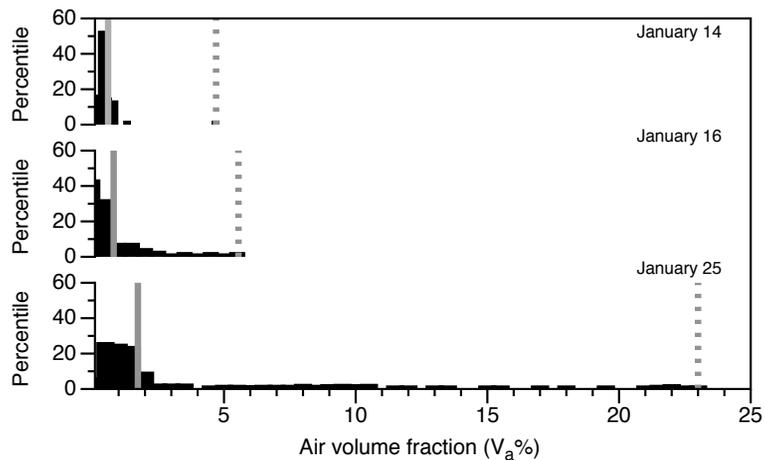
Figure 5. Shows the distribution of air volume fraction values computed for every 0.6 mm thick slice of each ice core per sampling date; 14, 16 and 25 January. The solid grey line is the mean air volume fraction and the dotted grey line show the maximum air volume fraction value observed for each sampling date.
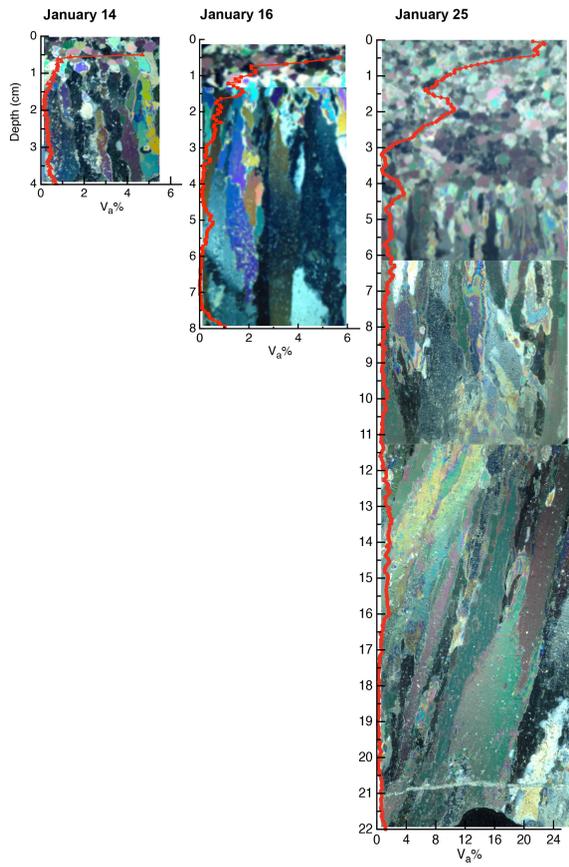
Figure 6. The ice microstructure compared to the air volume fraction (red curve) for 14, 16 and 25 January. The *x* scale differs for each date in order to visualize vertical change.
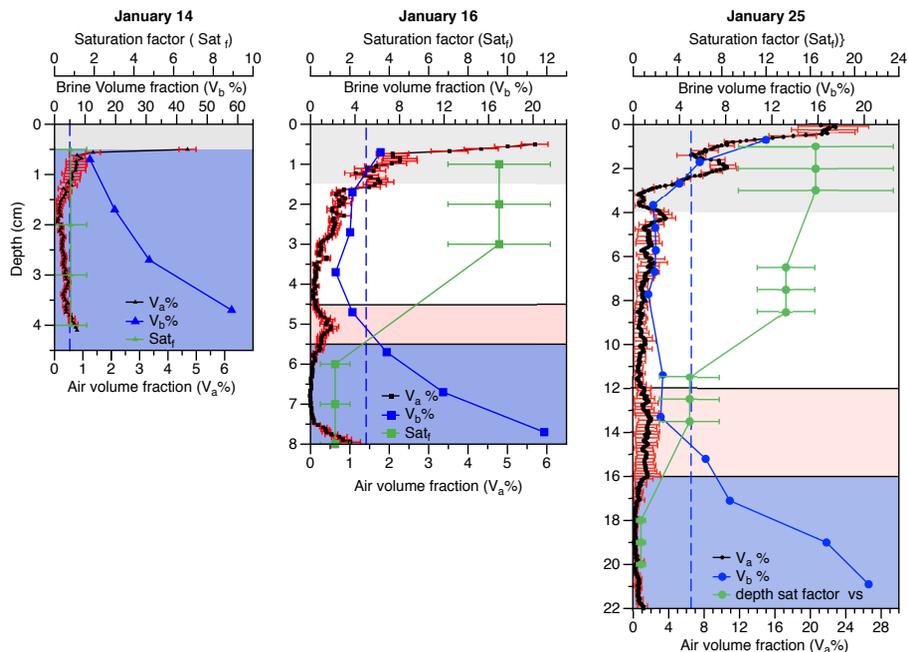
Figure 7. The vertical distribution of the air volume fraction in the ice cover for 14,16 and 25 January; the red error bars are the standard deviation of mean of the three selected threshold. The air volume fraction is compared to the brine volume fraction in blue and to the saturation factor in green. The dotted blue line is a reference value for the permeability threshold following Golden et al. (1998, 2007). The grey area represents the extend of the granular ice layer and the blue area represents the subsaturated ($SAT_f \leq 1$) and permeable ($V_b > 5\%$) bottom of sea ice in which the gas content is under or close to the theoretical concentration at atmospheric concentration. The red shaded area show a local V_a maximal at the transition between permeable and impermeable ice. Both the X and Y scale differ in order to visualize vertical change.
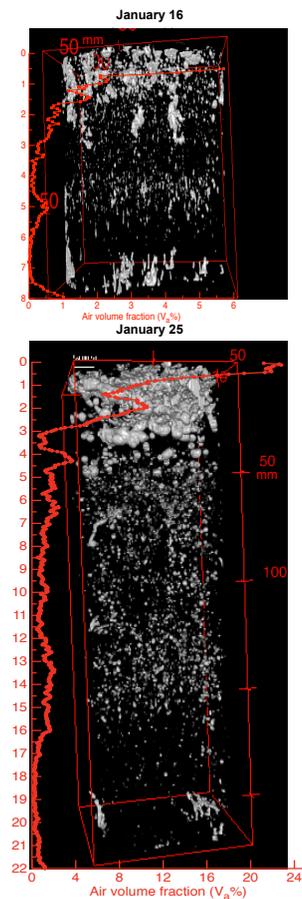
Figure 8. 3-D representations of the air inclusions for 16 and 25 January as compared to the air volume fraction (red curve).

Title Page

Abstract | Introduction

Conclusions | References

Tables | Figures

|◄ | ►|

◄ | ►

Back | Close

Full Screen / Esc

Printer-friendly Version

Interactive Discussion
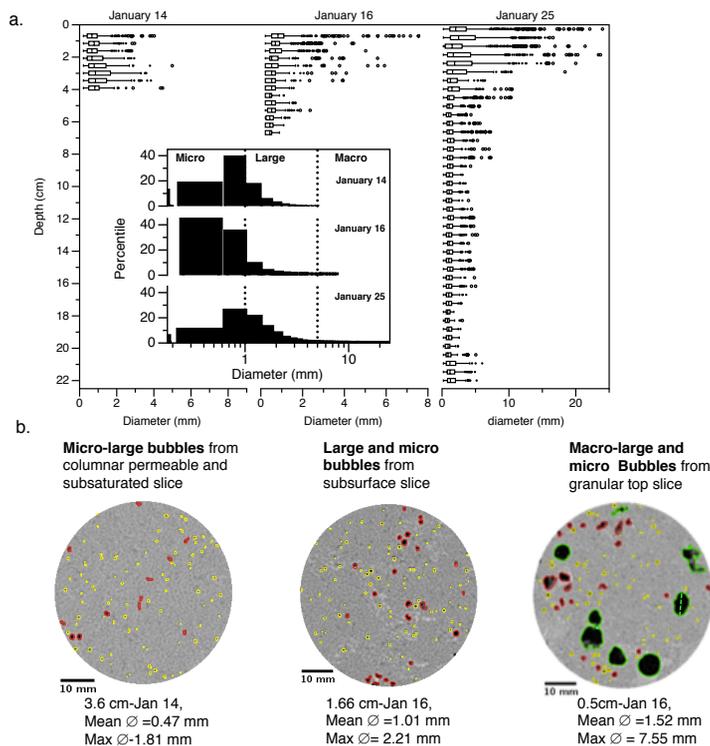
Figure 9. (a) the vertical distribution of the bubble diameters (i.e. air inclusions), the inside panel shows the histogram of the bubble diameters (i.e. air inclusions) per ice core sampled. **(b)** shows transversal slice at different depth containing micro (yellow), large (red) and macro (green) bubbles (i.e. air inclusions).

Full Screen / Esc

Printer-friendly Version

Interactive Discussion
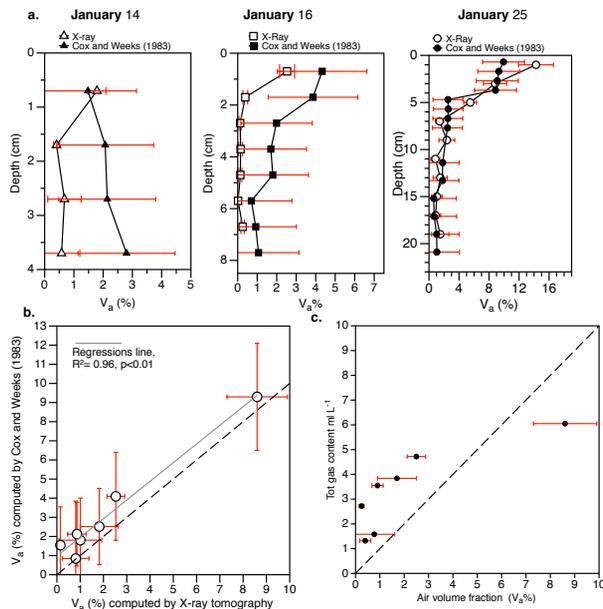
Figure 10. (a) Profile of the air volume fraction deduced from state equation of Cox and Weeks (1983) (plain symbol) using temperature, bulk ice salinity data and bulk density measurements, the error bar show the standard deviation from the mean of the results. The precision of air volume fraction computed from Cox and Weeks (1983) is strongly dependent of the precision of the density measurements. It's compared to the air volume fraction computed by CT X-ray tomography (white symbol), the error bars show the standard deviation of mean of the three selected threshold. **(b)** shows the relationship between the air volume fraction computed by CT-X-ray tomography and the air volume fraction deduced from Cox and Weeks (1983), the dotted line is the 1 : 1 relationship. **(c)** shows the relationship between the air volume fraction computed by CT-X-ray tomography and the bulk ice total gas content measured by gas chromatography, the dotted line is the 1 : 1 relationship.

a.

Number of Bubbles mm^{-2}

Air Volume fraction (V$_a$ %)

Mean Bubble diameter (mm)
- <0.25
- 0.25-0.5
- 0.5-0.75
- 0.75-1
- 1-2
- >2

Ice microstructure
- ▲ Jan 14 Granular
- ◁ Jan 14 columnar
- ◨ Jan 16 Granular
- □ Jan 16 columnar
- ◑ Jan 25 Granular
- ○ Jan 25 Columnar

b.

Bubbles percentil

- Micro porosity
- Large porosity
- Macro porosity

Cumulated air volume fraction (V$_a$%)

14 Jan 16 Jan 25 Jan
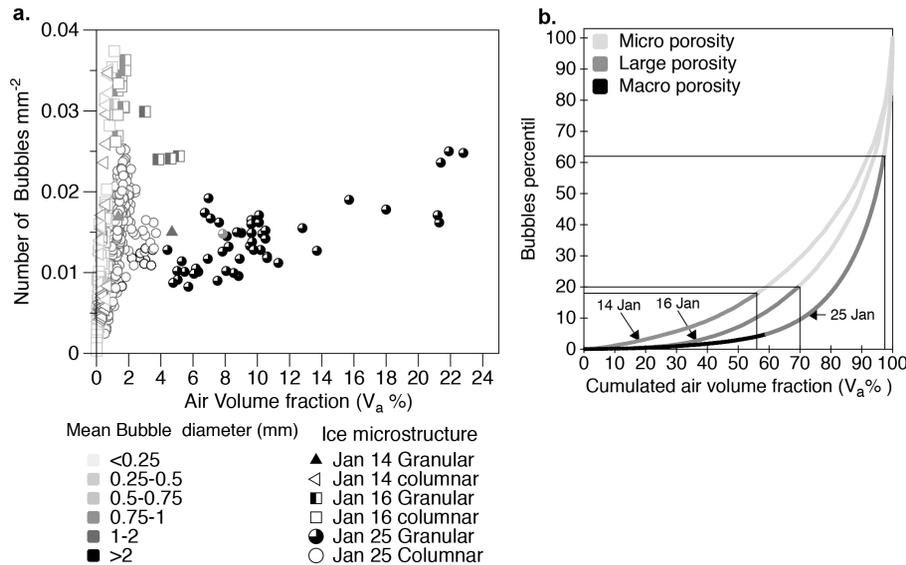
Figure 11. (a) shows the relationship between bubble density (number of bubbles per mm^{-2}, slice area) and air volume fraction (air volume fraction per slice) in function of both size of the bubbles (grey scale) and categorized by the type of sea ice microstructure (symbol, granular and columnar). **(b)** shows bubbles percentile contribution to the cumulated relative air volume fraction in % (100% means all observed CT air volume fraction is covered for a given core), categorized by bubble type (macro, large, micro) i.e. porosity type. It shows that, as time goes by, a smaller number (low percentile) of larger bubbles (e.g. macro on 25 January) results in a larger cumulated air volume fraction.
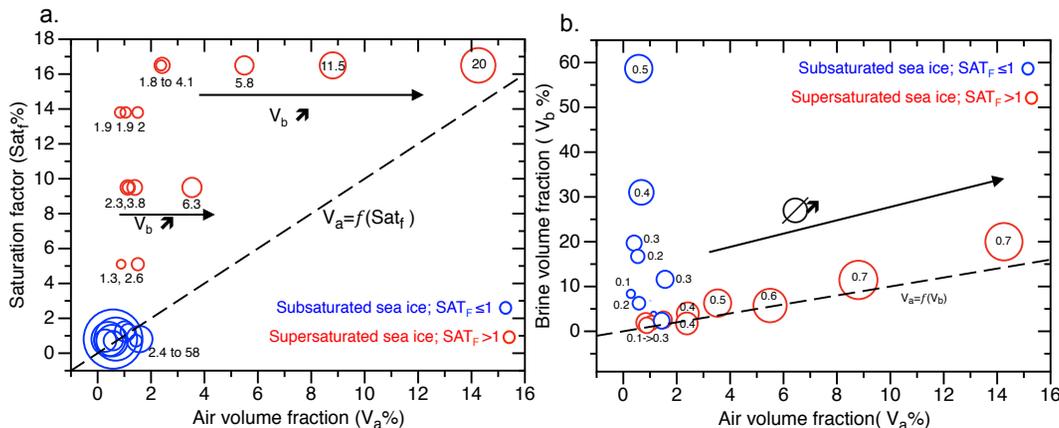
Figure 12. (a) shows the relationship between the air volume fraction and the level of saturation into the ice in function of the brine volume fraction, the size of circle is a function of the brine volume fraction, %. We differentiated the subsaturated ice ($SAT_f \leq 1$, blue circle) from the supersaturated ice ($SAT_f > 1$, red circle). For example, at high saturation level ($SAT_f = 16$), we observe higher air volume fraction when the brine volume fraction is higher. Within subsaturated ice the air volume fraction is always low regardless of the brine volume fraction. **(b)** shows the relationship between brine volume fraction and air volume fraction in function of the bubble diameter, the size of the circle is a function of the percentage of the bubble whose the diameter is higher than 1 mm. We differentiated the subsaturated ice ($SAT_f \leq 1$, blue circle) from the supersaturated ice ($SAT_f > 1$, red circle). Then within subsaturated ice the air volume fraction is always low regardless of the brine volume fraction. Within supersaturated ice, while the brine volume fraction increases the air volume fraction increased as well as the proportion of bubble with radii higher than 1 mm.
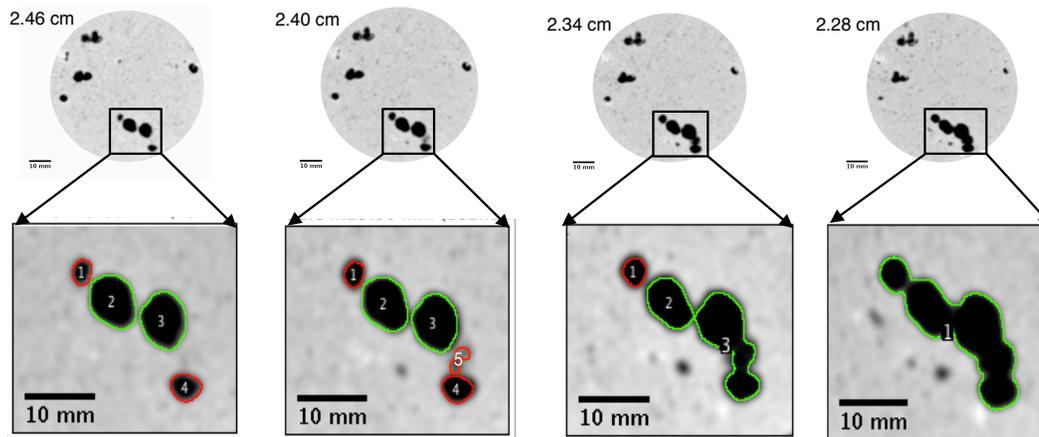
Figure 13. Shows the formation of macro bubble by coalescence processes from four successive slices in the frazil layer of 25 January.

Title Page

Abstract | Introduction

Conclusions | References

Tables | Figures

|◄ | ►|

◄ | ►

Back | Close

Full Screen / Esc

Printer-friendly Version

Interactive Discussion